

WAVEFRONT SHAPING ASSISTED DESIGN AND APPLICATION OF  
EFFECTIVE DIFFRACTIVE OPTICAL ELEMENTS PROVIDING SPECTRAL  
SPLITTING AND SOLAR CONCENTRATION:  
SPLICONS

A THESIS SUBMITTED TO  
THE GRADUATE SCHOOL OF NATURAL AND APPLIED SCIENCES  
OF  
MIDDLE EAST TECHNICAL UNIVERSITY

BY

BERK NEZİR GÜN

IN PARTIAL FULFILLMENT OF THE REQUIREMENTS  
FOR  
THE DEGREE OF MASTER OF SCIENCE  
IN  
PHYSICS

SEPTEMBER 2020



Approval of the thesis:

**WAVEFRONT SHAPING ASSISTED DESIGN AND APPLICATION OF  
EFFECTIVE DIFFRACTIVE OPTICAL ELEMENTS PROVIDING  
SPECTRAL SPLITTING AND SOLAR CONCENTRATION:  
SPLICONS**

submitted by **BERK NEZİR GÜN** in partial fulfillment of the requirements for the degree of **Master of Science in Physics Department, Middle East Technical University** by,

Prof. Dr. Halil Kalıpçılar  
Dean, Graduate School of **Natural and Applied Sciences**

\_\_\_\_\_

Prof. Dr. Altuğ Özpıneci  
Head of Department, **Physics**

\_\_\_\_\_

Assist. Prof. Dr. Emre Yüce  
Supervisor, **Physics, METU**

\_\_\_\_\_

**Examining Committee Members:**

Prof. Dr. Hamza Kurt  
Electrical and Electronics Engineering, TOBB ETÜ

\_\_\_\_\_

Assist. Prof. Dr. Emre Yüce  
Physics, METU

\_\_\_\_\_

Prof. Dr. Bülent Akınođlu  
Physics, METU

\_\_\_\_\_

Date: 21.09.2020



**I hereby declare that all information in this document has been obtained and presented in accordance with academic rules and ethical conduct. I also declare that, as required by these rules and conduct, I have fully cited and referenced all material and results that are not original to this work.**

Name, Surname: Berk Nezir Gün

Signature :

## ABSTRACT

### WAVEFRONT SHAPING ASSISTED DESIGN AND APPLICATION OF EFFECTIVE DIFFRACTIVE OPTICAL ELEMENTS PROVIDING SPECTRAL SPLITTING AND SOLAR CONCENTRATION: SPLICONS

Gün, Berk Nezir

M.S., Department of Physics

Supervisor: Assist. Prof. Dr. Emre Yüce

September 2020, 44 pages

The diffractive optical elements that mainly concentrate light are primarily designed via numerical methods. These methods incur increased computational time as well as a lack of real-life conditions. Our experimental approach offers a new design method for SpliCon, a particular type of diffractive optical element that can spectrally split and concentrate broadband light (420 nm - 875 nm). We managed to form a programmable SpliCon by wavefront shaping via a phase-only spatial light modulator. The method we adopted is  $\sim 300$  times faster than the conventional methods. We spectrally split the broadband range into three frequency bands, as well as achieving simultaneous concentration of the incident light. The spatial light modulator steered the frequency bands of red (560 nm - 875 nm), green (425 nm - 620 nm), and blue (420 nm - 535 nm) into two and three regions. When we have two concentration regions, the total enhancement factor is 715 %; and the spectral splitting ratios are 52 %, 57 %, and 66 % for the red, the green, and the blue channels, respectively. For the three concentration region case, the total enhancement factor is 564 %; and the spectral splitting ratios are 43 %, 37 %, and 34 % for the red, the green, and the

blue channels, respectively. Additionally, we present the methods to convert a programmable SpliCon into a physical Splicon that can be fabricated at large scale and low cost.

**Keywords:** wavefront shaping, diffractive optical elements, spectral splitting, solar concentration



## ÖZ

# SPEKTRAL BÖLME VE GÜNEŞ IŞIĞI KONSANTRASYONU SAĞLAYAN ETKİLİ KIRINIM OPTİK ELEMANLARIN DALGAÖNÜ ŞEKİLLENDİRME DESTEKLİ TASARIMI VE UYGULAMASI: SPLİCONLAR

Gün, Berk Nezir

Yüksek Lisans, Fizik Bölümü

Tez Yöneticisi: Dr. Öğr. Üyesi. Emre Yüce

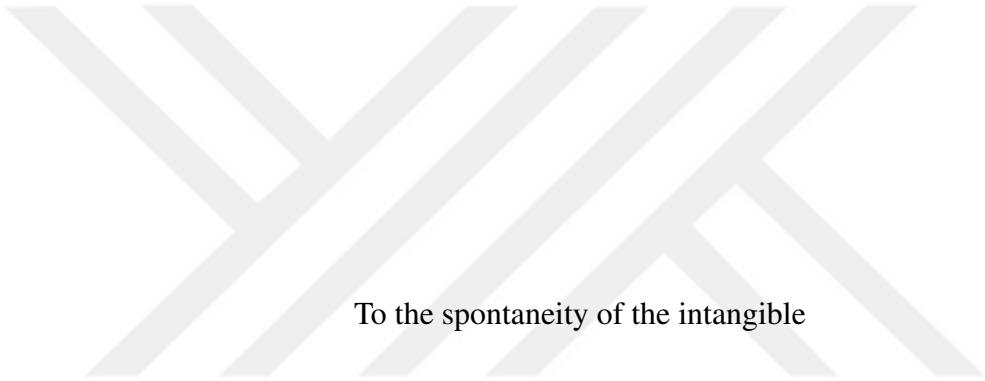
Eylül 2020 , 44 sayfa

Esas olarak ışığı yoğunlaştıran kırınımsal optik elemanlar öncelikle sayısal yöntemlerle tasarlanmıştır. Bu yöntemler, artan hesaplama süresinin yanı sıra gerçek yaşam koşullarının etkisini göz önünde bulundurma yönünden eksiklerdir. Deneysel yaklaşımımız, geniş bant ışığı (420 nm - 875 nm) spektral olarak bölebilen ve konsantre edebilen özel bir kırınım optik eleman türü olan SpliCon için yeni bir tasarım yöntemi sunar. Sadece faz modülasyonu sağlayan uzaysal ışık modülatörü ile dalga cephesini şekillendirerek programlanabilir bir SpliCon oluşturmayı başardık. Benimsediğimiz yöntem geleneksel yöntemlerden  $\sim 300$  kat daha hızlıdır. Geniş bant aralığını spektral olarak artan yoğunluk seviyeleri ile üç frekans bandına böldük. Mekansal ışık modülatörü, kırmızı (560 nm - 875 nm), yeşil (425 nm - 620 nm) ve mavi (420 nm - 535 nm) frekans bantlarını iki ve üç bölgeye yönlendirdi. İki konsantrasyon bölgemiz olduğunda, toplam geliştirme faktörü % 715'tir; ve spektral bölme oranları sırasıyla kırmızı, yeşil ve mavi kanallar için % 52, % 57 ve % 66'dır. Üç konsantrasyon bölgesi durumunda, toplam geliştirme faktörü % 564'tür; ve spektral bölme oranları sırasıyla

kırmızı, yeşil ve mavi kanallar için % 43, % 37 ve % 34'tür. Çalışmamızda ayrıca programlanabilir bir Splicon'u büyük ölçekte ve düşük maliyetle üretilebilen fiziksel bir Splicon'a dönüştürme yöntemlerini de sunuyoruz.

Anahtar Kelimeler: dalgaönü şekillendirme, kırınımsal optik elemanlar, tayfsal ayırılma, güneş ışığı konsantrasyonu





To the spontaneity of the intangible

## ACKNOWLEDGMENTS

I would like to express my deep gratitude to my advisor Assist. Prof. Dr. Emre Yüce for providing encouragement and guidance during this study. I would like to thank the members of the Programmable Photonics Group for their friendship.

I acknowledge the financial support supplied by The Scientific and Technological Research Council of Turkey (TÜBİTAK), grant no 118F075.

I want to thank my family for their unconditional support. I also want to thank my partner Beyza Durusoy for making me feel being loved. I appreciate my cats Müjgan & Müjde for sharing many moments with me. Thank you all for your naive existence.

## TABLE OF CONTENTS

ABSTRACT . . . . .	v
ÖZ . . . . .	vii
ACKNOWLEDGMENTS . . . . .	x
TABLE OF CONTENTS . . . . .	xi
LIST OF TABLES . . . . .	xiii
LIST OF FIGURES . . . . .	xiv
LIST OF ABBREVIATIONS . . . . .	xvii
CHAPTERS	
1 INTRODUCTION . . . . .	1
1.1 Diffractive optical elements . . . . .	3
1.2 Spatial light modulator . . . . .	7
1.3 In this thesis: . . . . .	8
2 THEORY . . . . .	11
2.1 Disturbances in space-time . . . . .	11
2.1.1 One dimensional wave equation . . . . .	11
2.1.2 Spherical wave equation . . . . .	12
2.2 Scalar theory of diffraction in diffractive optical elements . . . . .	14
2.2.1 Brief history of scalar theory of diffraction . . . . .	14

2.2.2	The Huygens-Fresnel principle in cartesian coordinates . . . .	15
2.2.3	Aperture function for phase elements . . . . .	16
3	INSTRUMENTATION AND METHODS . . . . .	19
3.1	Introduction . . . . .	19
3.2	Calibration . . . . .	19
3.3	Noise measurement . . . . .	23
3.4	Main Setup . . . . .	23
3.5	Optimization Algorithm . . . . .	25
4	RESULTS AND DISCUSSION . . . . .	27
4.1	Spectral splitting and concentration of broadband light . . . . .	27
4.1.1	Three frequency bands onto two target regions . . . . .	27
4.1.2	Three frequency bands onto three target regions . . . . .	33
4.1.3	Summary . . . . .	36
5	CONCLUSION . . . . .	39
	REFERENCES . . . . .	41

## LIST OF TABLES

### TABLES

Table 4.1 Enhancement factors as a function of # of iteration. The averages of three different datasets are used to find each value. The enhancement factor increases with the iterations. The data of the third iteration are processed in Fig. 4.3(a) yields a very close value to saturation of the enhancement factor (Fig. 4.3(b)). . . . .	32
Table 4.2 Spectral splitting ratios as a function of # of iteration. The averages of three different datasets are used to find each value. The data of the third iteration are processed in Fig. 4.3(c). . . . .	33
Table 4.3 Enhancement factors as a function of # of iteration. The averages of three different datasets are used to find each value. The enhancement factor increases with the iterations. The data of the third iteration are processed in Fig. 4.5(a). . . . .	36
Table 4.4 Spectral splitting ratios as a function of # of iteration. The averages of three different datasets are used to find each value. The data of the third iteration are processed in Fig. 4.5(b). . . . .	37

## LIST OF FIGURES

### FIGURES

Figure 1.1	Global weighted average levelized cost of energy and auction/ppa prices for concentrating solar power, onshore and offshore wind, and solar PV, 2010 to 2023. This figure is directly taken from [1]. . . . .	2
Figure 1.2	Refraction dominated interaction (a) is regarding the corpuscular theory of light whereas diffraction dominated interaction (b) is regarding wave theory of light. . . . .	3
Figure 1.3	When some portion of the light beam is blocked (a), it loses intensity. Interference occurs after diffraction when the light goes through small apertures (b). An incident monochromatic light beam might have different phase values such as $\pi$ and $\frac{3}{2}\pi$ after visiting a phase modulator. The phase of light at a specified target location can be altered by manipulating small apertures' related properties. . . . .	5
Figure 1.4	An SLM with various phase levels onto it. A CCD camera is facing towards the SLM. . . . .	8
Figure 2.1	Spherical coordinates . . . . .	13
Figure 2.2	Wavefronts (plane in this case) turn into spherical wavefronts after diffraction. They create a diffraction pattern at any observation point. . . . .	15
Figure 2.3	(a) A seven height step diffractive optical element. (b) A seven refractive index computer generated hologram . . . . .	17

Figure 3.1	The laser emits a 632.8 nm wavelength light beam. After being polarized, the light beam hits the SLM surface. After passing through the natural density filter, a coherent light beam reaches to the camera. . . . .	20
Figure 3.2	Some of the diffraction gratings on the SLM. Half of the diffraction grating pixels are fixed to black; the other ones are running towards white. . . . .	20
Figure 3.3	Systematic alteration of a specific set of diffraction grating stripes yields various diffraction orders. (a) $0^{th}$ diffraction order. (b) $0^{th}$ , $-1^{st}$ and $+1^{st}$ diffraction orders. The data of red squared ( $+1^{st}$ ) diffraction order will be presented together with the $0^{th}$ diffraction order in the next figure. (c) only the $0^{th}$ diffraction order is available for a certain gray level. (d) various diffraction orders seen at higher gray levels. . . . .	21
Figure 3.4	Irradiation change with respect to gray levels at the diffraction plane. (a) $0^{th}$ and (b) $1^{st}$ diffraction order visibilities as a function of gray level. . . . .	22
Figure 3.5	The 5-6 sequence is used for modulation at 633 nm for default voltages. Figure is directly taken from [2]. . . . .	22
Figure 3.6	A thermal sensor is positioned after the condenser lens for noise measurement of fiber connected broadband light. . . . .	23
Figure 3.7	The experimental setup to achieve spectral splitting and concentrating of broadband light. A beam of light is emitted from the fiber connected broadband light source, which is placed upper left side of the optical bench. Passing through the condenser lens, light is reflected from the mirror and gets linearly polarized before reaching the SLM (lower right of the optical bench). The light then passes through the positive lens and loses its partial intensity by visiting the density filter before impinging on the camera. . . . .	24

Figure 4.1	(a) The experimental setup that is used to mimic the elements able to concentrate and spectrally split broadband light onto particular target regions: SpliCons via SLM. The light source coupled to the fiber (F) emits a broadband light, it passes through condenser lens (C) with the focal length of 160 mm, and linear polarizer (P) placed on the path before SLM. A plano-convex lens (L) with the focal length of 300 mm is positioned to send the image on the SLM surface to the camera. (b) Image before the modulation of the wavefront. (c) Image after the modulation. (d) Final phase pattern on the SLM that spectrally splits and concentrates the white light. The images seen in panels (b) and (c) are the raw images acquired from the CCD camera. . . . .	28
Figure 4.2	Monochromatic intensity profile (a) before, (b) after wavefront shaping via SLM. Differential intensity changes for monochromatic, blue, green, and red channels are shown in panels (c), (d), (e), and (f), respectively. . . . .	29
Figure 4.3	The enhancement factor of spectral intensities as a function of (a) number of superpixels and (b) number of main iterations with 1024 adjustable superpixels. The spectral splitting ratio for each channel as a function of (c) number of superpixels (d) number of main iterations with 1024 adjustable superpixels. The error bars are within the physical size of the symbols shown in all panels. . . . .	30
Figure 4.4	Monochromatic intensity profile (a) before, (b) after wavefront shaping via SLM. Differential intensity changes for monochromatic, blue, green, and red channels are shown in panels (c), (d), (e), and (f), respectively. . . . .	34
Figure 4.5	The enhancement factor (a) and the spectral splitting ratio (b) of spectral intensities as a function of number of superpixels. The error bars are within the physical size of the symbols shown in all panels. . .	35

## LIST OF ABBREVIATIONS

3D	3 Dimensional
CGH	Computer Generated Hologram
DMD	Digital Micromirror Device
DOE	Diffraction Optical Element
LCoS	Liquid Crystal on Silicon
SLM	Spatial Light Modulator
SpliCon	Spectral Splitter and Solar Concentrator
PV	PhotoVoltaic



## CHAPTER 1

### INTRODUCTION

Since the very beginning of time, living beings have been dependent on energy sources by sustaining chain reactions of molecules to survive. The sun, a vast energy source of our planet, provides plants the light necessary to produce organic molecules and oxygen to sustain life. Apart from its biological importance, solar energy has one remarkable advantage over conventional energy sources, which is, being a truly renewable energy resource. That enabled us to use solar cells as an electricity source through the invention of the first practical photovoltaic (PV) cell [3]. The use of conventional energy resources (coal, oil, natural gas) is cost-effective, but drawbacks are apparent; they are not replenished at the same rate they used, and they are contributing to greenhouse gas emissions. Filtering greenhouse gases is necessary to prevent climate change and acid rain, but it increases electricity costs. These facts lead scientists to research more into renewable energy technologies. With the advances in technology, scientists have developed and implemented many tools that increase the efficiency of PV cells. Consequently, the cost of energy by using solar PV technology is under the fossil-fuel cost range. It will continue to decrease according to the estimations (Fig. 1.1).

The cost of electricity powered by PV systems decreases with the increasing efficiency of the system. There are two basic ways to boost the efficiency of a solar cell. The first one is material science. Each material combinations in PV cells use particular wavelength range to realize the photovoltaic effect, and each efficiency is different. Utilizing tandem solar cells, users can benefit from different spectra within the sunlight at the same time. This type of solar cells are a kind of multi-junction solar cells, and are formed by placing the materials that have different band gap energies

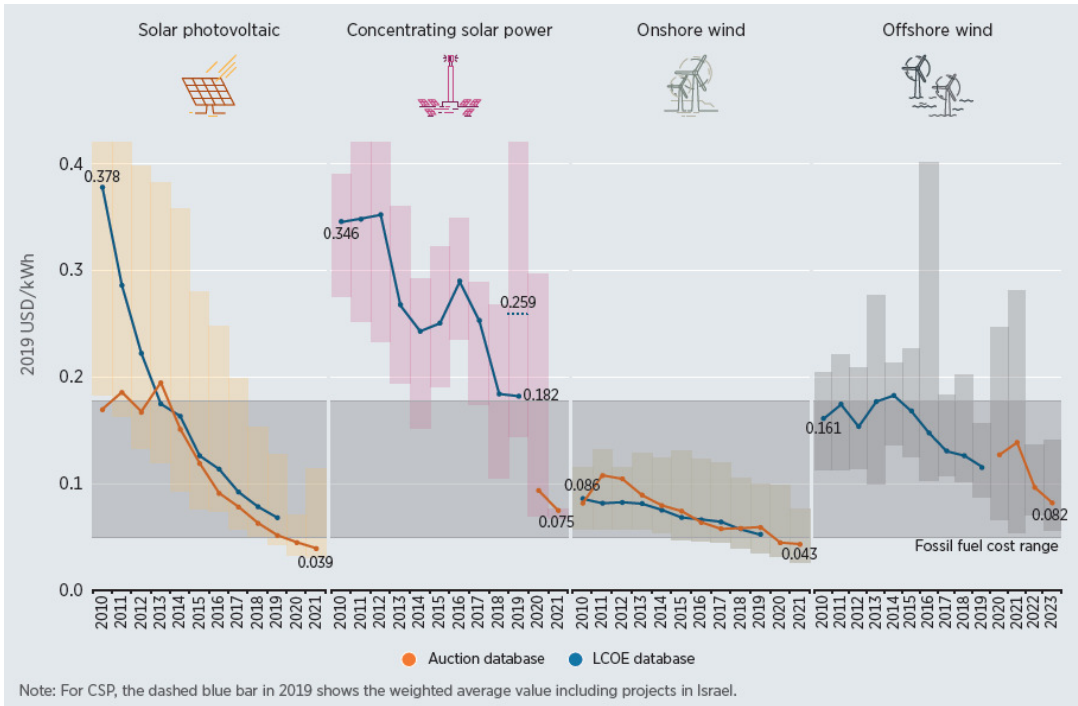


Figure 1.1: Global weighted average levelized cost of energy and auction/ppa prices for concentrating solar power, onshore and offshore wind, and solar PV, 2010 to 2023. This figure is directly taken from [1].

on top of each other systematically. Together with particular materials, the tandem solar cell itself can be considered as a spectral splitter. Although tandem solar cells have the efficiency record [4], they are currently not convenient due to their high cost and complex manufacturing process. Solar cells that employ lenses as a concentrator focus light on the desired region. In this case, efficiency depends on both material science and spatial control of light. Another efficient solar technology is the solar trackers which has the ability to capture sunlight from sunrise to sunset. The tracking mechanism moves to catch the light at the right angle that gives the highest efficiency. Using thin-film filters, users can filter out any undesired frequency bands to prevent thermalization decreasing efficiency [5]. As a spectral splitting method, prism assisted PV systems can be used with the concentrator materials [6]. Unfortunately, the PV system becomes bulky and costly. Benefits from that method require using certain types of PV cells because they have geometrical constraints resulting from the nature of dispersion.

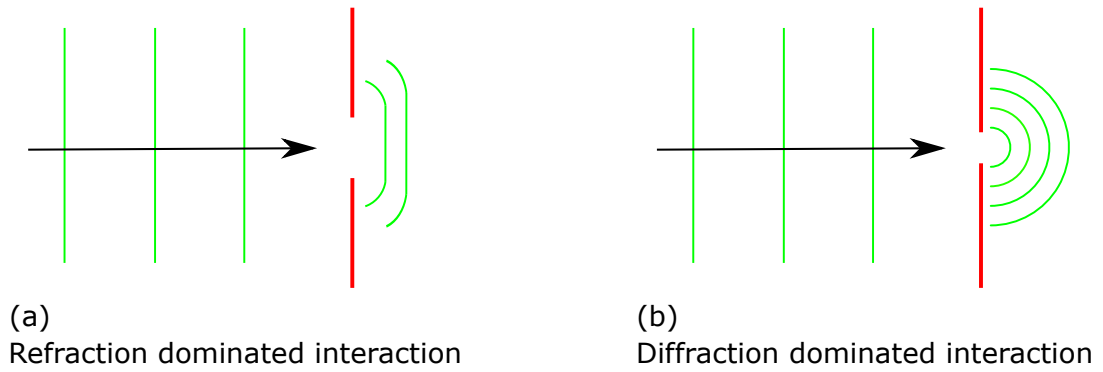


Figure 1.2: Refraction dominated interaction (a) is regarding the corpuscular theory of light whereas diffraction dominated interaction (b) is regarding wave theory of light.

The essential spectral splitting method is using diffractive optical elements (DOEs). These elements can be used in front of the laterally placed multi-junction solar cells. Unlike the tandem cells, DOE plays the splitter role and the cost of the splitting technology along with laterally placed multi-junction solar cells is not so expensive. Unlike the prism-assisted techniques, light passing through a DOE is in the diffraction regime rather than the refraction regime (Fig. 1.2). Interference effects are boosted by many pixels on a DOE, and the light phase can be fine-tuned using phase element on top of micro/nano-sized pixels. That method is so effective that spectral splitting and concentration of broadband light is achievable with a single element.

## 1.1 Diffractive optical elements

The general optical elements are either reflective or refractive such as mirrors, lenses, and beam splitters. For some applications, people incorporate diffractive instruments into their systems to utilize their remarkable benefits. A lens as a refractive instrument has only one focal point. However, in a diffractive optical element, users specify how many different focal points they want to profit. Thus, the concentration of incoming light without any intensity loss is possible in theory. However, there is a tiny drawback that puts some constraint on the diffraction efficiency of a DOE. This drawback is that the fabrication of a perfect blazed grating DOE is impossible due to the need of infinite number of height levels [7]. The number of height levels producible on a

DOE is limited. Fortunately, the diffraction efficiency is very close to 100 % for 16 and 32 height levels [8].

With the DOE technology it is possible to concentrate light on a significant degree [9]. Additionally, DOEs are very compact, considering the optical elements that are able to do a similar job together. DOE can be used in the field of laser material processing to split and shape laser beams for drilling or cutting material [10]. DOEs are also used in the position sensors and the motion detectors as well as lidar applications [11]. An essential application of DOE is in the biomedical field since it can be used as a diagnostics or treatment instrument. Some details about this application will be shortly given in the next section. In the communications field, DOE can be utilized as a spectral splitter to benefit from particular wavelength ranges. Apart from those applications, DOEs play a vital role in splitting white light falling onto the multi-junction PV cells. In Giang Nam Nguyen's doctoral thesis [12] he has made a precise DOE classification.

- Basic characteristic of a DOE

**Amplitude:** Amplitude modulation is realized by blocking or absorbing the incoming light. It negatively affects the DOE's diffraction ability.

**Phase:** No blocking of light within any DOE pixel. Interference between pixels (diffraction in our case) determines the concentration spot.

- Direction that light travels after hitting DOE w.r.t. light source

**Transmissive:** No reflectance within DOE. The diffraction plane is on the other side.

**Reflective:** The diffraction plane is on the same side as the light source. The reflectance of a DOE might decrease by moving away from the design wavelength.

- Thickness of a DOE

**Thick:** The phase shift induced by a DOE pixel height should be a lot greater than  $2\pi$ .

**Thin:** The phase shift induced by a DOE pixel height should be  $\sim 2\pi$ . Thin element approximation will be discussed in the next chapter.

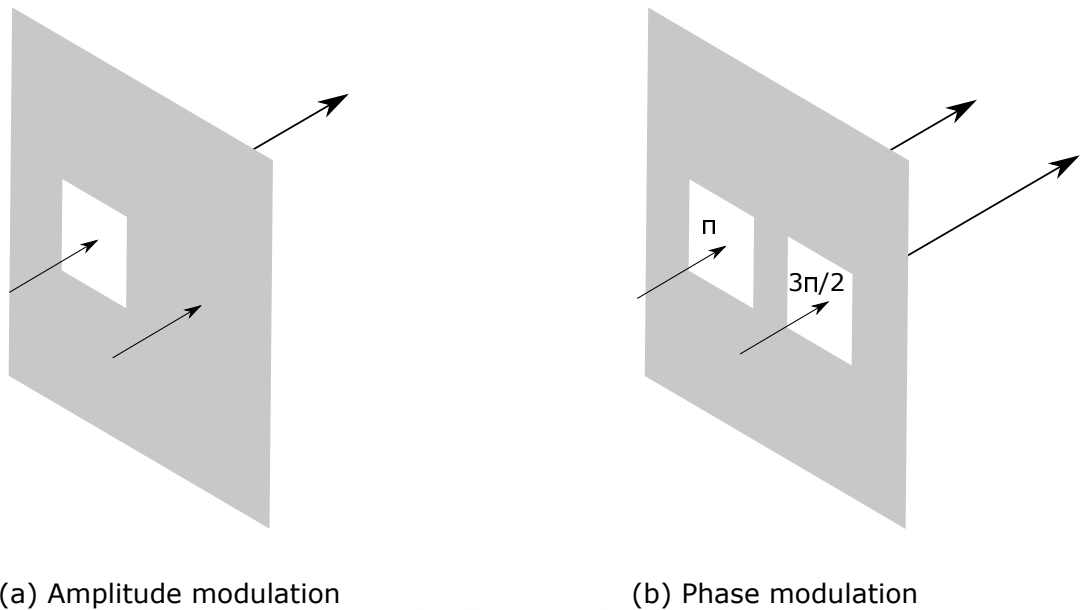


Figure 1.3: When some portion of the light beam is blocked (a), it loses intensity. Interference occurs after diffraction when the light goes through small apertures (b). An incident monochromatic light beam might have different phase values such as  $\pi$  and  $\frac{3}{2}\pi$  after visiting a phase modulator. The phase of light at a specified target location can be altered by manipulating small apertures' related properties.

- Theories in the creation of DOE

**Scalar paraxial models:** Small-angle approximation makes this scalar model less complicated than others.

**Scalar non-paraxial models:** No constraint exists in the scalar theory of diffraction.

**Vectorial theory:** For a more accurate calculation, vector components of the electromagnetic field is used. This theory can be utilized for a thick element DOE.

- The distance of diffraction plane w.r.t. DOE

**Near:** If a DOE can converge light, a diffraction pattern is observed at the near-field and this DOE is considered as a Fresnel element.

**Far:** The diffraction pattern is observed at the far-field and the DOE gives rise to it considered as a Fourier element. We will introduce a far-field approximation for the scalar theory of diffraction in the next chapter.

Traditionally, scientists use numerical methods to create a computer-generated hologram (CGH) to embody a DOE. These methods are related to which type of DOE that the user wants to have. In general, a DOE can be realized in three steps. The first step includes computational details such as setting the number of sampling points on both object and diffraction plane, and which type of theory that the programmer wants to use. The second step is about how to represent a CGH at the diffraction plane for the fabrication. The final step is the disclosure of encoded information of CGH for the fabrication device of DOE [9]. Some of the methods for DOE creation are Gerchberg-Saxton [13], Yang-Gu [14], direct binary search [15], iterative Fourier transform [16], genetic optimization [17] and simulated annealing [18]. Among these methods Gerchberg-Saxton gives the faster result. However, the efficiency stays limited [19]. Apart from the computational methods given above, CGHs can be produced faster via a spatial light modulator (SLM), experimentally. After that, this CGH can be reformatted (check Eq. 2.20) to fabricate it as a DOE.

We can expand the first step of the realization of DOE. Using the white light, optimization of DOE with high concentration and splitting efficiencies is a challenging task. The experimental research conducted by Kim et al. [20], has shown that the spectral splitting of light with the help of a DOE having 1000 pixels in one dimension. Numerical methods have optimized the heights of the pixels on the DOE. However, working with solely one dimension cannot yield a full control over the splitting and concentration of the incident white light. For this reason, we call DOEs that can split and concentrate light as SpliCons. Various studies are using three dimensions via numerical methods. For example the white light of between 400 nm - 1100 nm is divided range at every 1 nm to use 700 particular wavelengths. A DOE with 1600 pixels with nine-pixel height levels would require  $\sim 10^7$  data points to be processed. That takes much time and it lacks real-life circumstances. Dividing the wavelength range at smaller numbers incurs time loss. Besides, it does not provide a realistic picture because of not having a camera that can sense each frequency levels without crosstalks between the frequency channels. Seeing that, Yolalmaz et al. [19], developed an effective bandwidth approximation method that significantly decreases computational time without losing significant splitting and concentration values. That study is more realistic; however, it would include more real-life parameters if an experiment was

conducted. Some real-life effects hinge on the spatial and temporal coherence of white light, the overlapping frequencies in the camera, or the diffraction efficiency loss from SLM due to not having an infinite number of phase levels.

## 1.2 Spatial light modulator

Spatial Light Modulator (SLM) (Fig. 1.4) is an electro-optical device that converts data provided by electromagnetic signals into the electronic format. A phase-only SLM, which has  $\sim 60$  Hz refresh rate, writes the images onto the surface of itself via programmable control, which is a significant experimental advantage. This feature offers increased control over what classically called photographs (CGH on SLM in our case), along with the fact that it is in the electronic environment without the necessity of doing any mechanical work. Digital Micromirror Device (DMD), which has a high-speed refresh rate (up to  $\sim 23$  KHz [21]), is a special type of SLM having movable mirrors. However, this type of SLM is unable to modulate the phase of the incoming light beam. A phase-only SLM has liquid crystals responding to applied voltages through its birefringent nature. Different voltages on this type of SLM correspond to various phase shifts, which depend on refractive indices. Voltage - phase shift relation can be either linear or nonlinear, and fortunately, it is adjustable for a specific wavelength.

Additionally, due to SLM's diffractive structure based on a lot of micro-sized pixels, diffractive dispersion induced by the shape of pixels is highly effective in modulating. In this thesis, we only consider the linear changes in the phase shift as a function of gray levels as if we use monochromatic light. The details will be expanded in Chapter 3. Some of the research fields that include SLM use are optical tweezers [22], linear/nonlinear microscopy [23], micro-processing of materials [24], adaptive optics [25], pulse shaping [26] and computer-generated holograms [27]. As a biomedical research application, Vellekoop and Mosk introduced an effective method to focus light inside a tissue by taking the advantage of reduced diffraction limit via complex media [28].

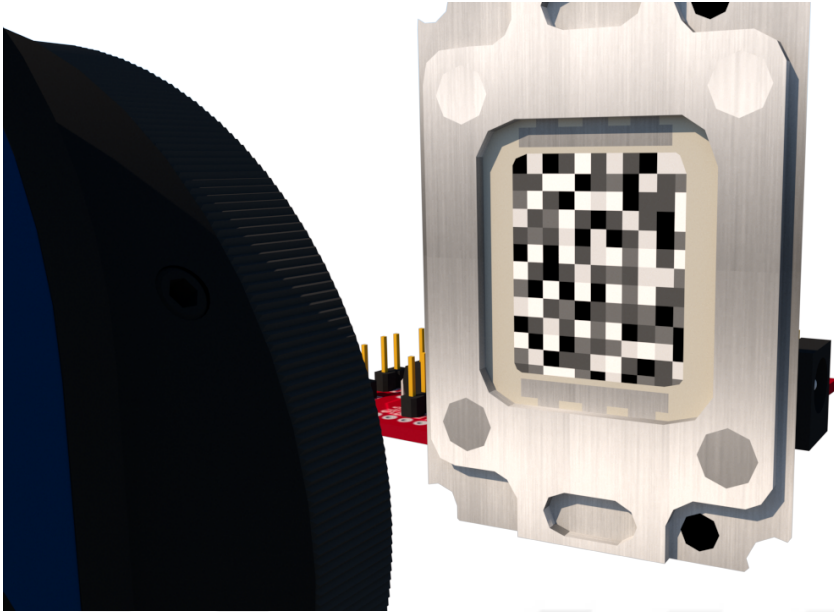


Figure 1.4: An SLM with various phase levels onto it. A CCD camera is facing towards the SLM.

### 1.3 In this thesis:

The purpose of this thesis is to spectrally split and concentrate the broadband light onto specified target regions via wavefront shaping. Previous studies focus on numerical DOE creation methods, but the presented study is the first experimental study that utilizes SpliCons for PV cell applications. We conducted experiments via a program that does not require high computational power. Besides, the program is adjustable for applying different experimental methods of focusing the incident light.

In the next chapter, we will provide information related to the theory of diffraction. There are different approaches and approximations in this theory, as stated in the diffractive optical elements section. We will expand the theory with its approximations to discuss our work. In the third chapter, we will reveal the details of how to use SLM properly by introducing the calibration process. We will also discuss how we utilized the instruments the way they used. We will introduce the main setup and the algorithm that we modified. In the fourth chapter, we will introduce our results for both two and three concentration regions and discuss the differences that arise from the way that the instruments used. In the conclusion section, we will discuss the

impact and draw an outlook.





## CHAPTER 2

### THEORY

#### 2.1 Disturbances in space-time

##### 2.1.1 One dimensional wave equation

$$\frac{\partial^2 \Psi(x, t)}{\partial t^2} = c^2 \frac{\partial^2 \Psi(x, t)}{\partial x^2}, \quad (2.1)$$

where  $x$  is the position,  $t$  the time,  $c$  the speed of light, and  $\Psi$  is the solution of the wave equation. This is a linear partial differential equation similar to heat equation or laplace equation.

$$\Psi(x, t) = f(x - ct) + g(x + ct), \quad (2.2)$$

Eq. 2.2 gives the general solution of the wave equation. Harmonic waves can be put to create a specific type of solution. It is also possible to show that where the harmonic wave solution comes. Since the wave equation is tough to solve, we need to use some tools to simplify it. If we consider the time and the space are entirely different parameters, we can apply the separation of variables to reduce it a known problem to solve.

$$\Psi(x, t) = u(x) v(t), \quad (2.3)$$

Placing it to the wave equation yields:

$$\frac{\partial^2 v(t)}{\partial t^2} = c^2 \frac{\partial^2 u(x)}{\partial x^2} = \lambda = -k^2, \quad (2.4)$$

There are three different solutions here, hinging on the value of  $\lambda$ . When  $\lambda < 0$ , the solution becomes:

$$\begin{aligned} \Psi(x, t) &= u(x) v(t) = [c_1 \cos(kx) + c_2 \sin(kx)][c_3 \cos(ckt) + c_4 \sin(ckt)], \\ &= A \exp[ik(x - ct)], \end{aligned} \quad (2.5)$$

Eq. 2.5 is in the format of Eq. 2.2 as expected.

### 2.1.2 Spherical wave equation

$$\frac{\partial^2 \Psi(r, \theta, \phi, t)}{\partial t^2} = c^2 \nabla^2 \Psi(r, \theta, \phi, t), \quad (2.6)$$

where  $\nabla^2$  is the laplacian operator. Expanding the laplacian in the spherical coordinates yields:

$$\nabla^2 = \frac{\partial^2}{\partial r^2} + \frac{2}{r} \frac{\partial}{\partial r} + \frac{1}{r^2} \frac{\partial^2}{\partial \theta^2} + \frac{\cot \theta}{r^2} \frac{\partial}{\partial \theta} + \frac{1}{r^2 \sin^2 \theta} \frac{\partial^2}{\partial \phi^2}, \quad (2.7)$$

where  $x = r \sin \theta \cos \phi$ ,  $y = r \sin \theta \sin \phi$  and  $z = r \cos \theta$ . For spherically symmetric waves, we can drop  $\theta$  and  $\phi$ .

$$\Psi(r, \theta, \phi) = \Psi(r), \quad (2.8)$$

The laplacian of  $\Psi(r)$  is:

$$\nabla^2 \Psi(r) = \frac{1}{r^2} \frac{\partial}{\partial r} (r^2 \frac{\partial \Psi}{\partial r}) = \frac{\partial^2 \Psi}{\partial r^2} + \frac{2}{r} \frac{\partial \Psi}{\partial r} = \frac{1}{r} \frac{\partial^2}{\partial r^2} (r \Psi), \quad (2.9)$$

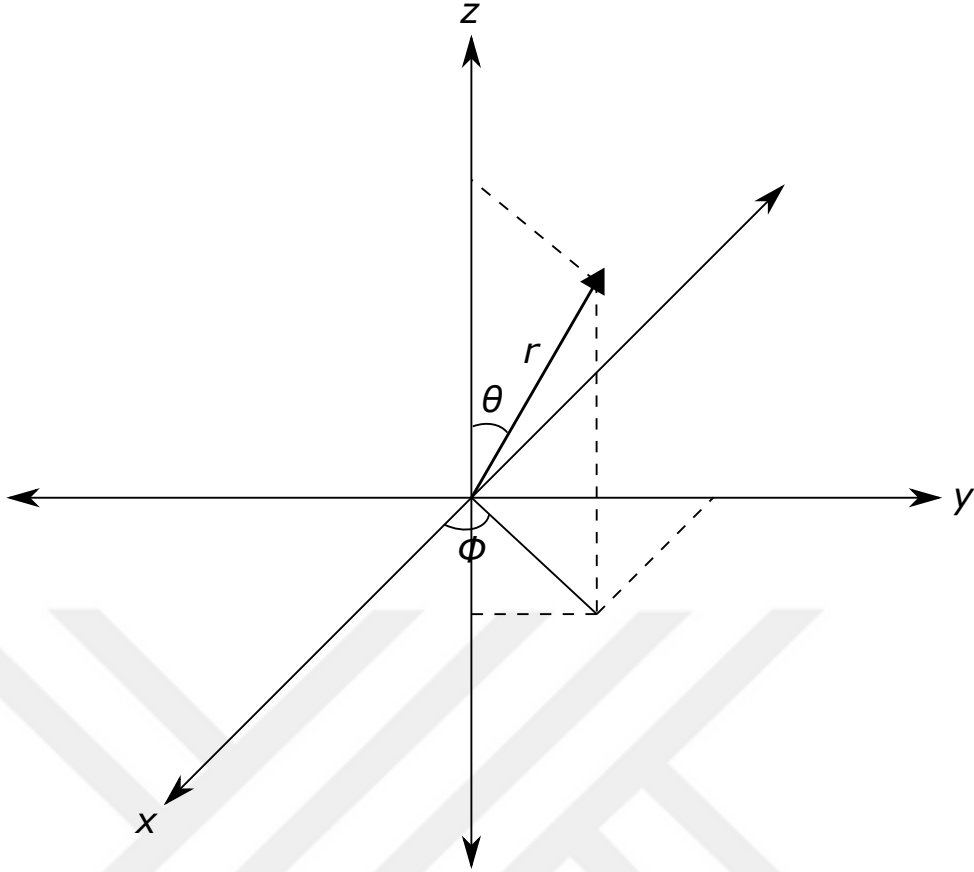


Figure 2.1: Spherical coordinates

by simplifying Eq. 2.9 we obtain:

$$\frac{\partial^2}{\partial r^2}(r\Psi) = \frac{1}{c^2} \frac{\partial^2}{\partial t^2}(r\Psi), \quad (2.10)$$

which has a similar form as we have in the one-dimensional wave equation in Eq. 2.1.

Hence the general solution will be in the form of:

$$\Psi(r, t) = A \frac{f(r - ct)}{r} + B \frac{g(r + ct)}{r}, \quad (2.11)$$

and we know that the harmonic wave solution exists. As a result, Eq. 2.11 will become:

$$\Psi(r, t) = \frac{A}{r} \exp[ik(r - ct)], \quad (2.12)$$

which is the spherically symmetric disturbance in space-time. This result will be used in the next section when we deal with Huygen's principle.

## **2.2 Scalar theory of diffraction in diffractive optical elements**

### **2.2.1 Brief history of scalar theory of diffraction**

Diffraction happens whenever a part of the wavefront encounters an obstacle whose dimensions are close to the radiation's wavelength. It was first accurately introduced by Francesco Maria Grimaldi (1618-1663), and his work was published in 1665, after two years from his death. He could have drawn more powerful conclusions such as observing light and dark fringes if he had studied with a light source that has more spectral purity. Christian Huygens (1629-1695) developed the theory by explaining how the fringes were formed in 1678. The effect that gives rise to fringes could not be explained by rectilinear propagation of radiation, which is explained by the corpuscular theory of light. Surprisingly, Isaac Newton (1643-1727), who had influenced scientists immoderately at his time, favored the corpuscular theory of light; thereby, there was no progress in the wave theory of light until the 19th century. English physician Thomas Young (1773-1829) introduced the interference phenomenon and developed the wave theory. Augustin Jean Fresnel (1788-1827) utilized the ideas of Huygens and Young and allowed wavelets to interfere with each other in his formulation [9]. The Huygens-Fresnel principle states that each point on a wavefront emanates spherical secondary wavelets [29]. The forward envelope of the secondary wavelets gives a new wavefront for any chosen time. James C. Maxwell (1831 - 1879), in 1860, put forward the idea that light is an electromagnetic wave. He introduced the vectorial approach that electric field and magnetic field vectors are dependent on each other [9]. In 1948 Dennis Gabor (1900 - 1979) found a novel wavefront construction method called holography [30]. He was awarded the Nobel Prize in Physics for his contribution to this field in 1971. Brown and Lohmann calculated the first CGHs in 1966 [31].

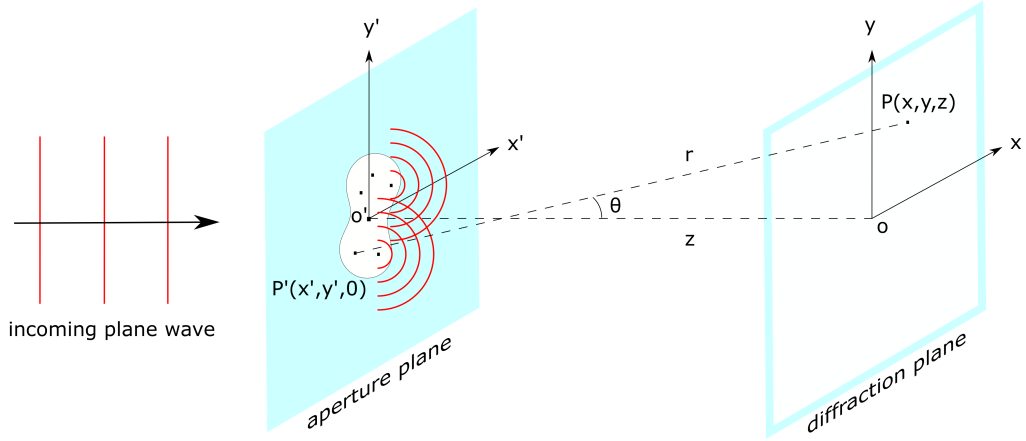


Figure 2.2: Wavefronts (plane in this case) turn into spherical wavefronts after diffraction. They create a diffraction pattern at any observation point.

### 2.2.2 The Huygens-Fresnel principle in cartesian coordinates

The Huygens-Fresnel principle (Eq. (2.13)) can be manipulated to determine the diffraction pattern in the near and the far-fields. Fig. 2.2 shows the plane wave impinging on the aperture plane where the aperture is small enough to reside in the diffraction regime. The incoming wave turns into spherical wavelets emitted from point sources within the aperture. We are looking for the light field for a specific point  $P(x,y,z)$  at the diffraction plane.

$$U(x, y, z) = \iint_{-\infty}^{\infty} \frac{1}{j\lambda} U(x', y', 0) \frac{e^{jkr}}{r} \cos\theta \, dx' \, dy' \quad (2.13)$$

where  $\cos\theta = \frac{z}{r}$ .  $U(x,y,z)$  is the field at point P on the diffraction plane due to the spherical wavelets coming from the aperture.  $U(x',y',0)$  is the aperture function whose value is between 0 and 1. Treating the problem with cartesian coordinates yields :

$$r = z \sqrt{\left(\frac{x-x'}{z}\right)^2 + \left(\frac{y-y'}{z}\right)^2 + 1} \quad (2.14)$$

Investigating the final light field within a small angle from the aperture, we use

parabolic approximation:  $|x - x'| \ll z$  and  $|y - y'| \ll z$ . By binomial approximation we rearrange r:

$$r = z \left( \frac{1}{2} \left[ \left( \frac{x - x'}{z} \right)^2 + \left( \frac{y - y'}{z} \right)^2 \right] + 1 \right) \quad (2.15)$$

Paraxial approximation yields  $r \cong z$ . However, this relation cannot be used for the exponential term in Eq. 2.13 due to the wave vector  $k$  being  $\approx 10^7 m^{-1}$  for the visible spectrum. Multiplying  $r$  with such a high value would reveal the difference between  $r$  and  $z$ . Putting  $r$  back into the equation:

$$U(x, y, z) = \frac{e^{jkz}}{jz\lambda} \iint_{-\infty}^{\infty} U(x', y', 0) \exp \left[ \left( \frac{jk}{2z} \right) (x - x')^2 + (y - y')^2 \right] dx' dy' \quad (2.16)$$

Expanding the quadratic phase function yields:

$$U(x, y, z) = \frac{e^{jkz} e^{\frac{jk}{2z}(x^2+y^2)}}{jz\lambda} \iint_{-\infty}^{\infty} U(x', y', 0) e^{\frac{jk}{2z}(x'^2-y'^2)} + e^{\frac{-jk}{z}(xx'-yy')} dx' dy' \quad (2.17)$$

Fraunhofer approximation ( $z \gg \frac{k}{2}(x'^2 + y'^2)_{max}$ ) alleviates the problem by shaping it for the far field:

$$U(x, y, z) = \frac{e^{jkz} e^{\frac{jk}{2z}(x^2+y^2)}}{jz\lambda} \iint_{-\infty}^{\infty} U(x', y', 0) e^{\frac{-jk}{z}(xx'-yy')} dx' dy' \quad (2.18)$$

The final field in this case is the Fourier Transform of the aperture function  $U(x', y', 0)$ .

### 2.2.3 Aperture function for phase elements

The aperture function is defined as the amplitude modulation function  $T(x', y', 0)$  multiplied by the possible phase shift in case of transmission.

$$U(x', y', 0) = T(x', y', 0) e^{j\Phi(x', y')} \quad (2.19)$$

In the diffractive optical element case, we have approximately %100 transmission through the aperture  $T(x',y',0) = 1$ . The phase element tunes the phase by shaping the wavefront. At the diffraction plane, monochromatic or specified polychromatic frequencies can be concentrated and/or spectrally split. During the transmission through the phase element, it is assumed that no diffraction occurs due to the phase element being thin [12]. Hence, the incoming light does not change its propagation direction. Now, we provide the path length formula for both DOEs and CGHs.

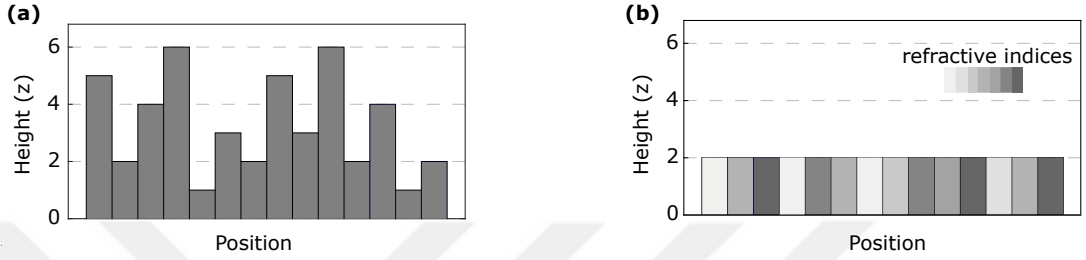


Figure 2.3: (a) A seven height step diffractive optical element. (b) A seven refractive index computer generated hologram

$$\phi_{xy}(\lambda) = \frac{2\pi}{\lambda} h_{xy} [n(\lambda) - 1], \quad (2.20)$$

where  $\phi_{xy}(\lambda)$  is the phase difference between the incident light restricted to go through the phase element inside the diffractive material and the incident light without encountering any element on the observer plane positioned at  $(x,y)$ . Considering the phase element interaction, we are taking neither diffraction nor law of refraction into account that changes the initial direction of incoming light.  $h_{xy}$  is the thickness of the phase element inside the diffractive material,  $n(\lambda)$  the phase element's refractive index,  $\lambda$  the wavelength of the incident light. In a DOE, the refractive index is fixed, whereas the thickness of DOE material is varied pixel by pixel (Fig. 2.3(a)). The pixel heights are fixed on SLM; thereby, modulation happens via altering the refractive indices (Fig. 2.3 (b)). By using the formula above, SLM pixels can be transformed into DOE pixels.



## CHAPTER 3

### INSTRUMENTATION AND METHODS

#### 3.1 Introduction

In this chapter, we introduce the instrumentation and methods used in this study to manage wavefront shaping via SLM. SLM, an electro-optic device that can alter the amplitude and phase of the incident light on pixels is a crucial component of our experiment. It consists of pixels at the order of  $\sim 10^6$ , and they are micrometers in size, providing diffraction domination rather than refraction. We controlled the voltages applied to each pixel so that we can control the amount of phase retardation. The more discrete phase levels that the SLM have, the better the tuning is. For creating desired phase differences, the testing (or calibration) of the SLM is essential.

#### 3.2 Calibration

In this section, we will measure the phase stability of SLM using monochromatic light. The basis of calibration of an SLM is based on the alleviation of the non-linear response of the refractive index changes in the birefringent material. Setting linear phase responses yields us to convert programmable Splicons into physical SpliCons in a further accurate way (check Eq. 2.20). This linearity highly depends on the wavelength used. In the cases where a broadband source is used, we can use the calibration method by can be utilized either setting the peak wavelength of the broadband source as calibration wavelength for getting linear responses or for mere validation of if SLM is working properly. Various phase levels are originated from the pulse code modulation in an SLM. In Fig. 3.5, the flicker of the used sequence measured at 633

nm is given [2]. The flicker arises from the phase instabilities due to limited viscosity in the liquid crystal molecules.

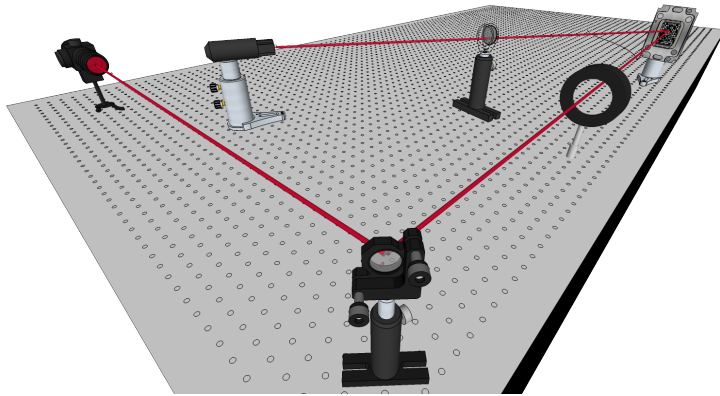


Figure 3.1: The laser emits a 632.8 nm wavelength light beam. After being polarized, the light beam hits the SLM surface. After passing through the natural density filter, a coherent light beam reaches to the camera.

To verify the information provided by the manual of the SLM [2], we setup the configuration, which is seen in Fig 3.1. Pluto-2-NIR-011 phase-only Liquid Crystal on Silicon (LCoS) microdisplay with full HD resolution of 1920 x 1080 parallel aligned nematic SLM, which can modulate wavelengths in between 420 nm and 1064 nm has been used with Thorlabs WP25M-UB wire grid polarizer to set particular polarization direction dictated by the manufacturer of the SLM. 632.8 nm and 5 mW maximum power output of Melles Griot HeNe Laser with the noise level around 15 %, Thorlabs NENIR10A absorptive neutral density filter with optical density 1.0 and Guppy Pro F-125C Camera have been used for this process.

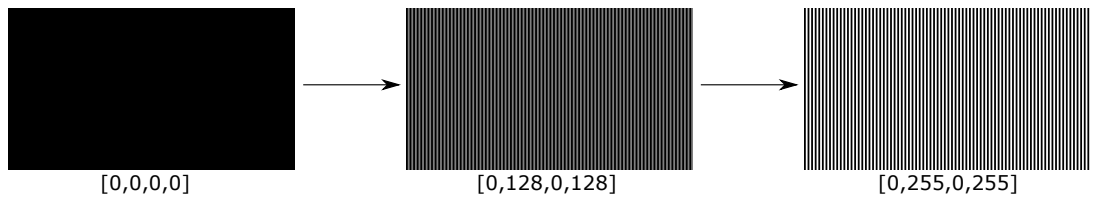


Figure 3.2: Some of the diffraction gratings on the SLM. Half of the diffraction grating pixels are fixed to black; the other ones are running towards white.

We have utilized a diffraction-based phase calibration method by encoding changing 256 particular diffraction gratings on the SLM consecutively. Each grating has two

different gray levels except the first grating (seen in Fig. 3.2 as  $[0,0,0,0]$ ). One of the gray levels has been fixed to black whereas the other gray level changes towards white as seen in Fig. 3.2. The diffraction gratings are  $1920 \times 1080$  in resolution and have 80 pairs of phase elements. The width of a line of the grating can be found as  $\sim 10^{-4}$  meters by taking SLM dimensions into account. Considering the typical beam width of laser is in between  $0.5 \times 10^{-3} \text{ m} - 10^{-3} \text{ m}$ , we can state that laser beam impinges on  $\sim 5 - 10$  line of grating, which is enough for modulation.

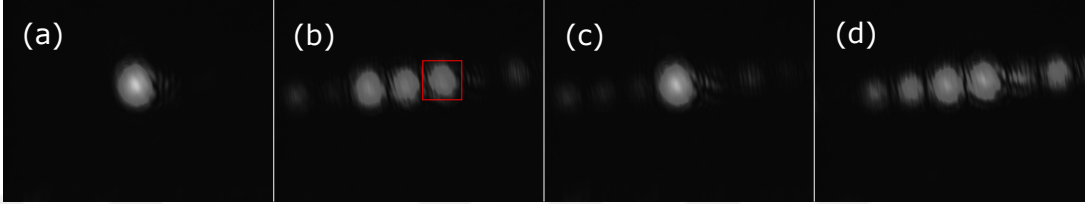


Figure 3.3: Systematic alteration of a specific set of diffraction grating stripes yields various diffraction orders. (a)  $0^{th}$  diffraction order. (b)  $0^{th}$ ,  $-1^{st}$  and  $+1^{st}$  diffraction orders. The data of red squared ( $+1^{st}$ ) diffraction order will be presented together with the  $0^{th}$  diffraction order in the next figure. (c) only the  $0^{th}$  diffraction order is available for a certain gray level. (d) various diffraction orders seen at higher gray levels.

Feeding the SLM surface with these diffraction gratings yields the images seen in Fig. 3.3. Some images show only the  $0^{th}$  diffraction order, whereas some contains higher diffraction orders. This change results from the spatial modulation. To quantify the phase modulation we have plotted the irradiance vs gray level graphs for both  $0^{th}$  and  $1^{st}$  diffraction orders which can be seen in Fig. 3.4.

In Fig. 3.4 panel (a) the graph indicates  $0^{th}$  diffraction order irradiance amounts as a function of gray level. Irradiance values are normalized with the maximum irradiance value of the  $0^{th}$  diffraction order. In panel (b)  $1^{st}$  diffraction order visibility is shown. The difference between the  $0^{th}$  and  $1^{st}$  order irradiance amount is explained with the diffraction efficiency of the SLM.

$$\eta = R.(1 - A).FF^2.\eta_H.\eta_{on} \quad (3.1)$$

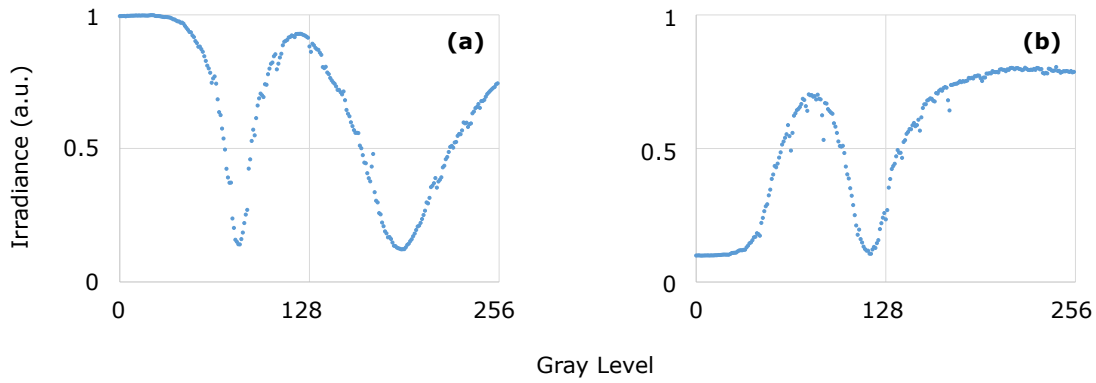


Figure 3.4: Irradiation change with respect to gray levels at the diffraction plane. (a)  $0^{th}$  and (b)  $1^{st}$  diffraction order visibilities as a function of gray level.

It depends on absorption effects by internal reflections inside an SLM (A), fill factor (FF) and mirror reflectivity (R) of SLM together with the efficiency of hologram ( $\eta_H$ ) and the fraction of usable time ( $\eta_{on}$ ) [32]. The phase shift is seen in Fig. 3.4 panel (a) is  $\sim 3.6\pi$ , and the data in panel (b) becomes ambiguous after  $3\pi$  modulation. Our data are compatible with the data provided by the manufacturer of the SLM.

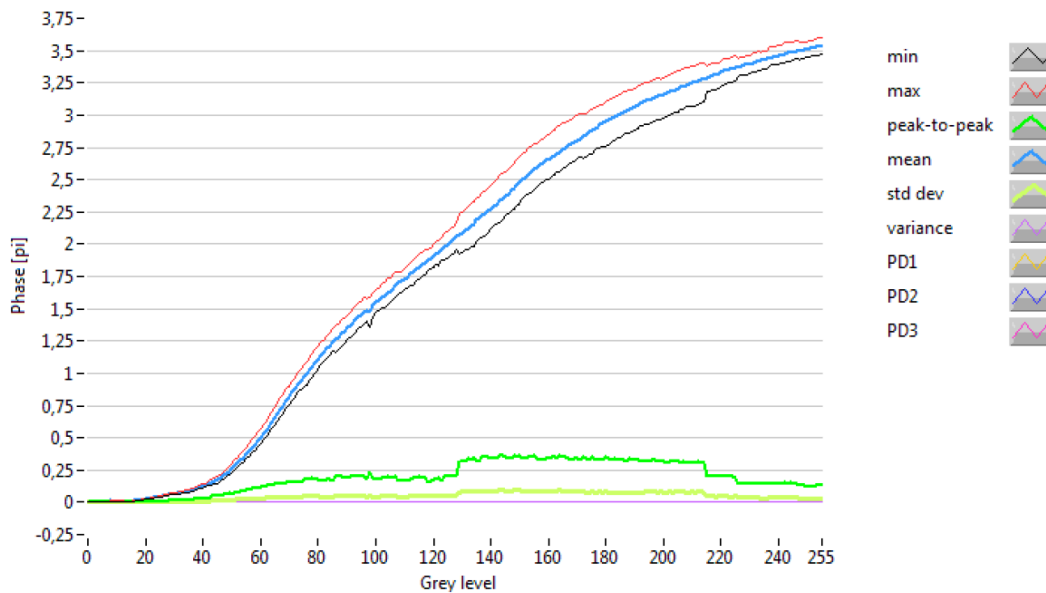


Figure 3.5: The 5-6 sequence is used for modulation at 633 nm for default voltages. Figure is directly taken from [2].

### 3.3 Noise measurement

To test Thorlabs SLS201L/M broadband light source (360 nm - 2600 nm) with a peak wavelength of 1000 nm, we prepared the setup shown in Fig. 3.6. The optical power of fiber-coupled stabilized tungsten-halogen broadband light was measured by a S401C thermal power sensor connected to the PM100D console positioned at 8 cm from the fiber placed immediately after the condenser lens, and the average power was 8.49 mW for 535 nm. The standard deviation of optical power was 0.4 %, acceptable compared to the stated value in the manual of the device [33]. Measurements were taken for one hour long.

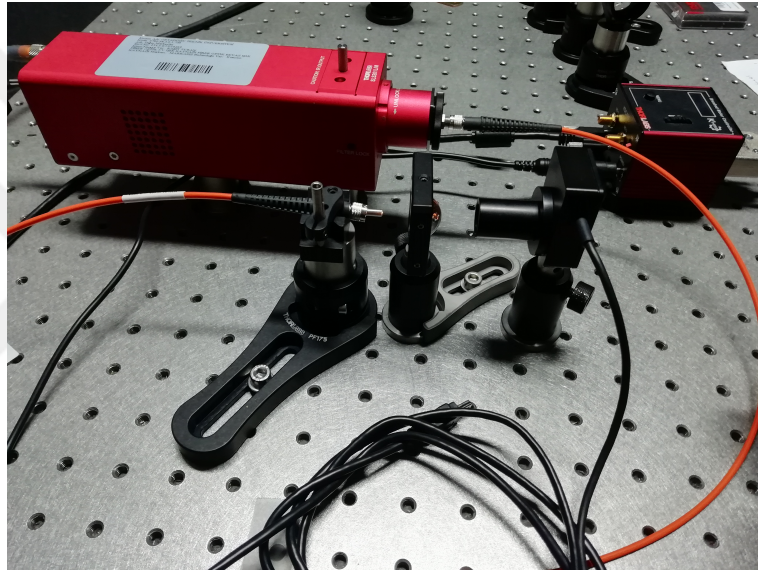


Figure 3.6: A thermal sensor is positioned after the condenser lens for noise measurement of fiber connected broadband light.

### 3.4 Main Setup

The light emitted from the fiber connected to the broadband source visits Thorlabs ACL 25416U-A aspheric condenser lens, Thorlabs PF10-03-M01-10 round protected gold mirror and Thorlabs WP25M-UB wire grid polarizer, respectively, before hitting on the SLM (Pluto-2-NIR-011 phase-only) surface. After reflecting from the SLM surface, the light goes into the Thorlabs LA1484 - N-BK7 Plano-Convex Lens

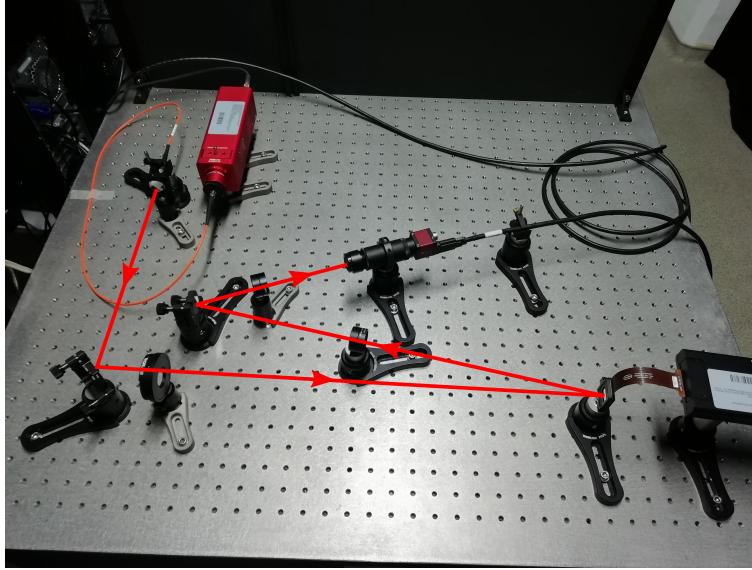


Figure 3.7: The experimental setup to achieve spectral splitting and concentrating of broadband light. A beam of light is emitted from the fiber connected broadband light source, which is placed upper left side of the optical bench. Passing through the condenser lens, light is reflected from the mirror and gets linearly polarized before reaching the SLM (lower right of the optical bench). The light then passes through the positive lens and loses its partial intensity by visiting the density filter before impinging on the camera.

( $f = 300$  mm). After being filtered by Thorlabs NENIR10A mounted NIR ND filter, modulated light arrives at the Guppy Pro F-125C Camera. The spectral responses provided by the manufacturer [34] of the camera are  $19.5 \times 10^{-2}$  A/W,  $18.0 \times 10^{-2}$  A/W and  $13.5 \times 10^{-2}$  A/W with the peak wavelengths at 610 nm, 535 nm, 450 nm for the red, green, and blue channels, respectively.

The SLM is connected to the computer, and its second virtual screen is created by the size of the SLM to dictate SLM, which phase patterns to encode on itself. We gather SLM pixels as superpixels to save a significant amount of time besides monitoring the effect of different superpixel sizes on the intensity captured. One of the outputs is the concentration and splitting of broadband light as a function of # of superpixels, which will be presented in the results chapter.

### 3.5 Optimization Algorithm

At first, the algorithm encodes 8-bit white for each pixel to monitor non-modulated light. It is important to recall that every phase element corresponds to different gray levels as indicated in the calibration section. We systematically create various phase differences on the SLM superpixels by starting from a particular edge. We have set 16 particular phase elements/gray levels to encode on the SLM. The more variety of phase elements provide more diffraction efficiency independent of the quality of the SLM. However, SLM noises originate from our camera hampering to detect little differences within an acceptable error margin. Additionally, 16 height level is much-used in the DOE technology and easy to fabricate. We have set two different target spots to steer different color channels onto them. The color channels are defined between 560 nm - 875 nm, 425 nm - 620 nm, and 420 nm - 535 nm for red, green, and blue channels, respectively. More information about the technical details will be provided in the related section of the following chapter.

The algorithm records all spectral intensity values onto the target spots and updates the SLM surface with the gray value giving the highest total intensity. We define that process as a sub-iteration and the algorithm's sub-iteration time is  $\sim 250$  ms. The sub-iteration time can actually be cut more than five times by considering the theoretical restrictions. After one sub-iteration is done, the algorithm scans the nearest superpixels towards a particular direction to dictate every sub-iteration happens. When each superpixel finds its gray value, a phase pattern emerges. This process is defined as the main iteration. The outcomes show differences with respect to iteration number, thereby one of our measurements gives the spectral splitting and concentration values as a function of # of iteration, and will be presented in the results chapter.



## CHAPTER 4

### RESULTS AND DISCUSSION

#### 4.1 Spectral splitting and concentration of broadband light

In this chapter, we are going to provide the data and the figures with the processed data that show both spectral splitting and concentration achievement. We put forward some definitions for spectral splitting and concentration and interpret the results in terms of these definitions. Mostly, the constraints created by the instruments and their effects on the experiment along with the question of how can we optimize the outcome will be the main focus for us. We investigate the spectral splitting and the concentration of broadband light using two and three target regions.

##### 4.1.1 Three frequency bands onto two target regions

Fig. 4.1(b) gives the raw irradiation data on the camera surface before the spatial modulation via wavefront shaping. The concentrated and spectrally split broadband light is seen in Fig. 4.1(c). This formed image is a consequence of different phase levels on the micro pixels of the SLM. The target region of the red and the green-blue frequency bands are centered at  $(x,y) = (1.07 \text{ mm}, 1.03 \text{ mm})$  and  $(3.32 \text{ mm}, 1.03 \text{ mm})$ , respectively. The modulation at the end is due to the phase pattern on the SLM, and is seen in Fig. 4.1(d) in the form of gray levels. This phase pattern is called as CGH and can be turned into physical SpliCon. We need to quantify the quality of wavefront shaping by defining some metrics before we introduce processed images. By defining  $\Delta I^k$ , we explicitly illustrate the images to emphasize the differences

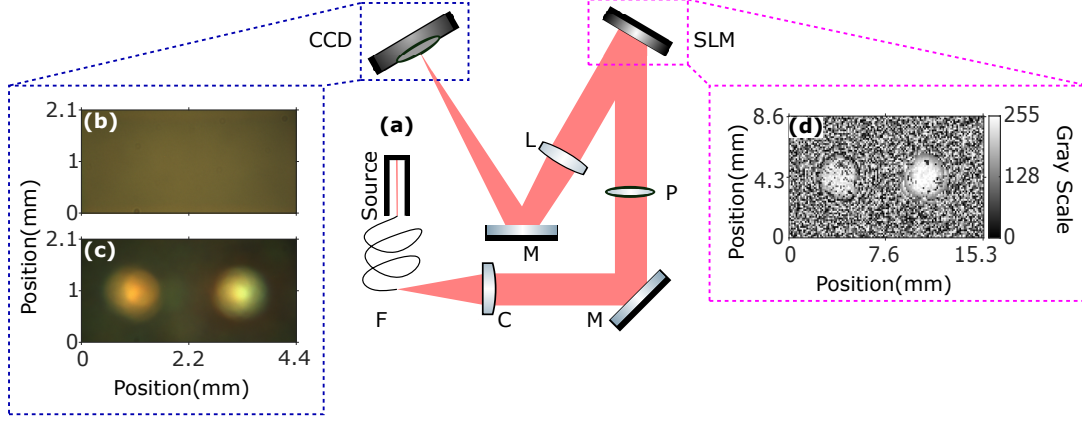


Figure 4.1: (a) The experimental setup that is used to mimic the elements able to concentrate and spectrally split broadband light onto particular target regions: SpliCons via SLM. The light source coupled to the fiber (F) emits a broadband light, it passes through condenser lens (C) with the focal length of 160 mm, and linear polarizer (P) placed on the path before SLM. A plano-convex lens (L) with the focal length of 300 mm is positioned to send the image on the SLM surface to the camera. (b) Image before the modulation of the wavefront. (c) Image after the modulation. (d) Final phase pattern on the SLM that spectrally splits and concentrates the white light. The images seen in panels (b) and (c) are the raw images acquired from the CCD camera.

between the non-optimized image and the optimized image via spatial modulation.

$$\Delta I^k(\lambda) = \frac{I_f^k(\lambda) - I_i^k(\lambda)}{I_i^k(\lambda)}, \quad (4.1)$$

where  $k$  is the pixel number and range between  $k = \{1, 2, \dots, n\}$ .  $I^k(\lambda)$  is the scalar-valued function showing spectral intensity values. The subscript  $i$  and  $f$  stand for the initial and final intensities, respectively. We also defined the enhancement factor to quantify the concentration quality.

$$\eta(\lambda) = \frac{\int_T I_f(A_m, \lambda) dA_m}{\int_T I_i(A_m, \lambda) dA_m}, \quad (4.2)$$

The enhancement factor is defined as the ratio of final spectral intensity on the target region of the chosen frequency band and incident spectral intensity on the target region of the same frequency band.  $A_m$  is the area of the  $m^{\text{th}}$  target region and

$m = \{1, \dots, l\}$  for the number of  $l$  target regions, respectively.  $\int_T I_i(A_m, \lambda) dA_m$  and  $\int_T I_f(A_m, \lambda) dA_m$  are the spectral intensities on a target region before and after wavefront shaping, respectively.

$$S(\lambda) = \frac{\int_T I_f(A_m, \lambda) dA_m}{\sum_{m=1}^l \int_T I_f(A_m, \lambda) dA_m}, \quad (4.3)$$

$S(\lambda)$  is spectral splitting ratio. It is defined as spectral intensity on the corresponding target region over the spectral intensity on each target region. The letter  $m$  is assigned to show target regions.

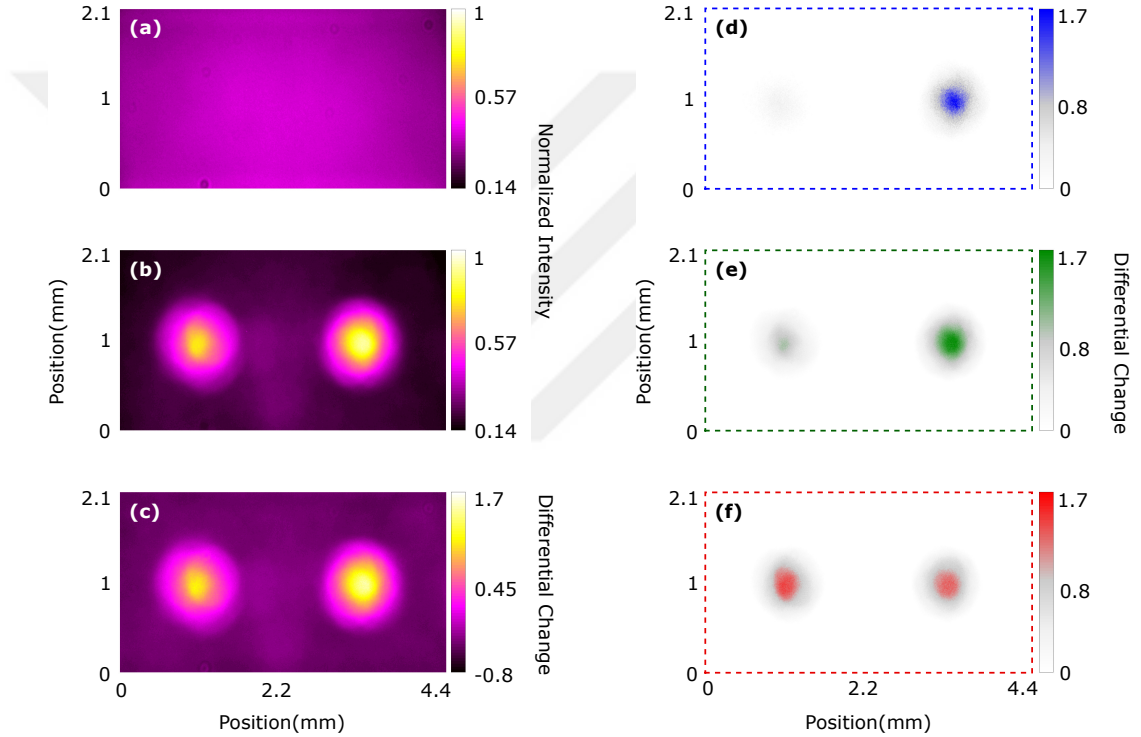


Figure 4.2: Monochromatic intensity profile (a) before, (b) after wavefront shaping via SLM. Differential intensity changes for monochromatic, blue, green, and red channels are shown in panels (c), (d), (e), and (f), respectively.

In Fig. 4.2 we replot the raw images as functions of both monochromatic and spectral channels. The monochromatic channel is formed by adding RGB channel intensities, and then normalized by the maximum intensity value. Fig. 4.2(a) and (b) show that the monochromatic intensity values of both before and after the optimization, respectively. In Fig. 4.2(c) we utilized the differential change (Eq. (4.1)) to see the differ-

ence clearly. In Fig. 4.2 panels (d-f), the differential change in the frequency channel of red (560 nm - 875 nm), green (425 nm - 620 nm), and blue (420 nm - 535 nm) are supplied. As is seen in panels (d) and (e), blue and green channels are concentrated on the right target region whereas the red channel concentration spot seems ambiguous (panel (f)). Alongside the visual elements introduced, mathematical quantities will be discussed with the help of the following figure. As a consequence of the upcoming analysis, the concentration region for the red channel will be revealed to be the left target region as desired. The reason for the visual ambiguity on the concentration region in panel (f) is the frequency overlap between different channels. At 5 % quantum efficiency, the green and the blue channels have approximately 66.7 % overlap, whereas the red and the green channels of the CCD chip have 29.3 % a overlap [34]. The latter suffices to increase the red channel intensity on the right target region, and this incurs a lower spectral splitting ratio for the red channel. Nonetheless,  $S(560\text{nm} - 875\text{nm}) > 0.5$  condition is still satisfied.

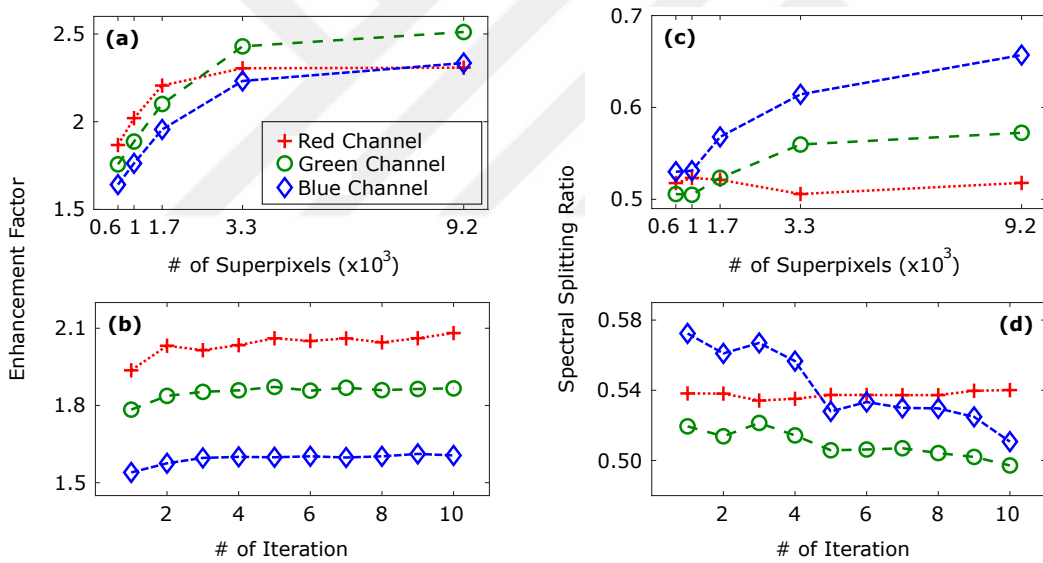


Figure 4.3: The enhancement factor of spectral intensities as a function of (a) number of superpixels and (b) number of main iterations with 1024 adjustable superpixels. The spectral splitting ratio for each channel as a function of (c) number of superpixels (d) number of main iterations with 1024 adjustable superpixels. The error bars are within the physical size of the symbols shown in all panels.

We present the enhancement factor and spectral splitting ratio data quantitatively in Fig. 4.3 as a function of # of superpixels and # of iteration. In all panels, we use

the mean of three different datasets with 16 phase steps. In the panels (a) and (c) we use three main iterations. In the panels (b) and (d), we use 1024 superpixels. In Fig. 4.3(a) the enhancement factor of the red channel decreases with the increasing # of superpixels whereas the green and the blue channel increase. Concentrating two different frequency bands onto a single target region is easier than concentrating only one frequency band to a target region. In our algorithm, we capture the total maximum intensity on the target regions. As our control over SLM increases, the intensity on the green-blue target region affects total maximum intensity more. As a consequence of this, the enhancement factors of the green and the blue frequency bands are higher than the red frequency band for 9216 superpixels that arise from the usage of 15 x 15 groups of SLM pixels. The reason for the red channel being the highest for the lower # of superpixels is the spectral responses of the camera.

We also present our first and second iteration data along with the third one to see the development of the enhancement factor in Table 4.1. As # of iteration increases, the enhancement factor also increases due not to reaching a possible saturation value. In Fig. 4.3(b), we monitor the change in the enhancement factors as a function of # of iteration by using only 1024 superpixels. The red frequency band has the most significant enhancement factor value due to using that amount superpixels. The enhancement factor values are saturated at  $\sim 5^{th}$  main iteration, although the subsequent iteration values are not much higher. We have a smooth graph, thanks to the constraints that we put inside our algorithm. The total enhancement factor for 9216 adjustable superpixels with three iteration is 715 %.

In Fig. 4.3 panels (c) and (d), we illustrate spectral splitting ratio responses. In panel (c), the blue channel spectral splitting ratio has an increasing trend together with the green channel spectral splitting ratio. The frequency overlaps dictated by the camera is the leading cause of lower spectral splitting ratios. The red channel has a decreasing trend because of its spectral response being the highest. This factor boosts the effect of frequency overlap between the red and the green frequency bands by increasing the red channel intensity on the green-blue target region. In Table 4.2, the development of spectral splitting ratios as a function of # of iteration is monitored. As the # of iteration increases, the red channel splitting ratio becomes dominant due to its highest spectral response (Fig. 4.3(d)). The spectral splitting ratios for 9216

Table 4.1: Enhancement factors as a function of # of iteration. The averages of three different datasets are used to find each value. The enhancement factor increases with the iterations. The data of the third iteration are processed in Fig. 4.3(a) yields a very close value to saturation of the enhancement factor (Fig. 4.3(b)).

Enhancement factors as a function of # of iteration				
# of Superpixels	$\eta(\lambda)$	1. iteration	2. iteration	3. iteration
$0.6 \times 10^3$	$\eta(\text{red})$	1.72	1.85	1.87
	$\eta(\text{green})$	1.64	1.73	1.76
	$\eta(\text{blue})$	1.56	1.63	1.64
$1 \times 10^3$	$\eta(\text{red})$	1.86	1.99	2.02
	$\eta(\text{green})$	1.74	1.85	1.89
	$\eta(\text{blue})$	1.64	1.74	1.76
$1.7 \times 10^3$	$\eta(\text{red})$	1.99	2.17	2.20
	$\eta(\text{green})$	1.85	2.02	2.10
	$\eta(\text{blue})$	1.73	1.90	1.96
$3.3 \times 10^3$	$\eta(\text{red})$	2.25	2.30	2.30
	$\eta(\text{green})$	2.16	2.40	2.43
	$\eta(\text{blue})$	1.99	2.19	2.23
$9.2 \times 10^3$	$\eta(\text{red})$	2.25	2.29	2.31
	$\eta(\text{green})$	2.10	2.38	2.51
	$\eta(\text{blue})$	1.97	2.21	2.33

adjustable superpixels with three iterations are 52 %, 57 %, and 66 % for red, green, and blue channels, respectively. Since the highest spectral response provides the most intensity on the target region, the green and the blue frequency bands decrease dramatically. To prevent sharp changes in the spectral splitting ratio, we can determine weights in the algorithm to equalize the spectral response rather than changing the camera settings due to affecting the quality of the image negatively. For the overlapping frequency problem, one can use a multi-spectral camera. In comparison with the CCD camera, a multi-spectral camera offers a couple of narrow frequency bands to

Table 4.2: Spectral splitting ratios as a function of # of iteration. The averages of three different datasets are used to find each value. The data of the third iteration are processed in Fig. 4.3(c).

Spectral splitting ratios as a function of # of iteration				
# of Superpixels	S( $\lambda$ )	1. iteration	2. iteration	3. iteration
$0.6 \times 10^3$	S(red)	0.52	0.51	0.51
	S(green)	0.50	0.50	0.50
	S(blue)	0.53	0.53	0.53
$1 \times 10^3$	S(red)	0.52	0.52	0.52
	S(green)	0.50	0.51	0.50
	S(blue)	0.53	0.53	0.53
$1.7 \times 10^3$	S(red)	0.53	0.53	0.52
	S(green)	0.51	0.52	0.52
	S(blue)	0.55	0.57	0.57
$3.3 \times 10^3$	S(red)	0.53	0.51	0.51
	S(green)	0.53	0.56	0.56
	S(blue)	0.58	0.62	0.61
$9.2 \times 10^3$	S(red)	0.56	0.53	0.52
	S(green)	0.53	0.56	0.57
	S(blue)	0.60	0.65	0.66

provide high-quality imaging.

#### 4.1.2 Three frequency bands onto three target regions

In this section we present our results for splitting and focusing three frequency bands onto three target regions. The figures presented here are processed exactly the same way that we do in the previous section. In Fig. 4.4 panels (a) and (b) we add intensities of individual channels to both depict the concentration regions and the difference between incident (a) and final intensity (b). Additionally, we implement the differ-

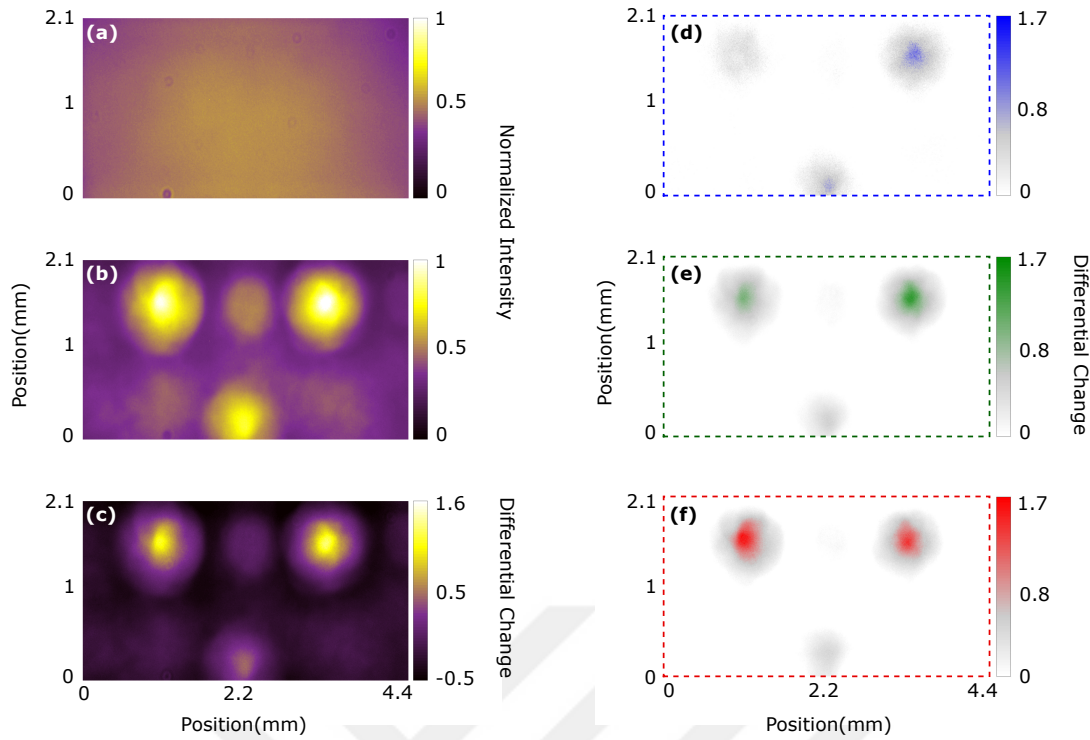


Figure 4.4: Monochromatic intensity profile (a) before, (b) after wavefront shaping via SLM. Differential intensity changes for monochromatic, blue, green, and red channels are shown in panels (c), (d), (e), and (f), respectively.

ential change operation to illustrate the intensity difference in one image, which is in panel (c). In panels (d), (e), and (f), we aim to show differential changes of individual frequency channels. From left to right, the target region of the red, the blue and the green frequency bands are centered at  $(x,y) = (1.07 \text{ mm}, 1.59 \text{ mm})$ ,  $(2.19 \text{ mm}, 0.09 \text{ mm})$  and  $(3.32 \text{ mm}, 1.59 \text{ mm})$ , respectively. Unfortunately, these concentration spots are not much distinguishable by the naked eye for two reasons. The first reason is that the different spectral responses of frequency channels of the camera. Due to the red channel having the highest spectral response, red channel differential change, which is seen in panel (f), is more intense than the other channels. The second reason is that we set the differential change limit the same for each channel. This prevents us from seeing which concentration region belongs to which frequency band by the naked eye. The blue channel intensity increases on the green channel target region (rightmost region) as well due to the overlapping frequencies between the blue and the green channels (Fig. 4.4(d)). The green channel intensity increases on the red

channel target region (leftmost region) because of the frequency overlap between the red and the green channel boosted by the spectral response of the red channel (Fig. 4.4(e)). The red channel intensity is seen in Fig. 4.4(f) increases on the green target region due to the overlapping frequencies between the red and the green channels. In fact, intensities increase on all target spots owing to the fact that there are no extra constraints in the algorithm that restricts the increase of other channel intensities for a chosen target region.

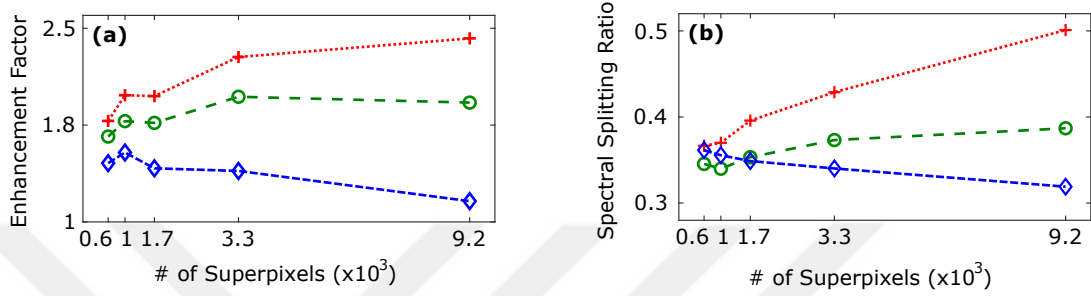


Figure 4.5: The enhancement factor (a) and the spectral splitting ratio (b) of spectral intensities as a function of number of superpixels. The error bars are within the physical size of the symbols shown in all panels.

In Fig. 4.5(a) from the highest enhancement factor to the lowest, red-green-blue alignment does not change as the # of superpixels increases in comparison with the outcomes that are presented in Fig. 4.3(a). In consequence of steering the broadband beam towards three particular target regions, the frequency bands with more spectral responses are higher in enhancement factor. The blue channel enhancement factor decreases due to having the lowest spectral response. The algorithm tries to maximize the intensity of the concentration regions, which affects the red channel intensity more than the others in the absence of weight functions. More detailed data can be found in Table 4.3, which contains first and second iteration data as well as the third one. We observe that we gain further control if we increase the adjustable superpixel amount on the SLM. The total enhancement factor for 3318 adjustable superpixels with three iterations is 564 %. In Fig. 4.5(b) the red channel spectral splitting ratio is the highest in comparison with the data shown in Fig.4.3(c). Here, the significance of overlaps between the channels is very low because each channel has its own target region. Hence, the parameter that shapes the metrics is the spectral response, predominantly. The spectral splitting ratios for 3318 adjustable superpixels with three iterations are

Table 4.3: Enhancement factors as a function of # of iteration. The averages of three different datasets are used to find each value. The enhancement factor increases with the iterations. The data of the third iteration are processed in Fig. 4.5(a).

Enhancement factors as a function of # of iteration				
# of Superpixels	$\eta(\lambda)$	1. iteration	2. iteration	3. iteration
$0.6 \times 10^3$	$\eta(\text{red})$	1.69	1.76	1.78
	$\eta(\text{green})$	1.59	1.65	1.66
	$\eta(\text{blue})$	1.41	1.44	1.46
$1 \times 10^3$	$\eta(\text{red})$	1.80	1.96	1.98
	$\eta(\text{green})$	1.68	1.77	1.78
	$\eta(\text{blue})$	1.48	1.51	1.54
$1.7 \times 10^3$	$\eta(\text{red})$	1.82	1.94	1.97
	$\eta(\text{green})$	1.66	1.74	1.77
	$\eta(\text{blue})$	1.43	1.38	1.42
$3.3 \times 10^3$	$\eta(\text{red})$	2.08	2.17	2.28
	$\eta(\text{green})$	1.79	1.88	1.97
	$\eta(\text{blue})$	1.56	1.40	1.39
$9.2 \times 10^3$	$\eta(\text{red})$	1.86	2.26	2.42
	$\eta(\text{green})$	1.53	1.82	1.92
	$\eta(\text{blue})$	1.19	1.16	1.16

43 %, 37 %, and 34 % for the red, the green, and the blue channels, respectively. Aggregate data can be found in 4.4.

### 4.1.3 Summary

We achieved spectral splitting and concentration for both two and three target spots for three frequencies. However, we have some differences in results. Total enhancement factors are 715 % and 564 % for two and three concentration regions, respectively. The reason that the former case yields higher results than the latter case is

Table 4.4: Spectral splitting ratios as a function of # of iteration. The averages of three different datasets are used to find each value. The data of the third iteration are processed in Fig. 4.5(b).

Spectral splitting ratios as a function of # of iteration				
# of Superpixels	S( $\lambda$ )	1. iteration	2. iteration	3. iteration
$0.6 \times 10^3$	S(red)	0.36	0.36	0.37
	S(green)	0.34	0.34	0.35
	S(blue)	0.35	0.35	0.36
$1 \times 10^3$	S(red)	0.37	0.37	0.37
	S(green)	0.34	0.34	0.34
	S(blue)	0.36	0.35	0.36
$1.7 \times 10^3$	S(red)	0.38	0.40	0.40
	S(green)	0.34	0.36	0.35
	S(blue)	0.36	0.34	0.35
$3.3 \times 10^3$	S(red)	0.41	0.42	0.43
	S(green)	0.34	0.36	0.37
	S(blue)	0.36	0.34	0.34
$9.2 \times 10^3$	S(red)	0.46	0.49	0.50
	S(green)	0.36	0.38	0.39
	S(blue)	0.34	0.32	0.32

the significant overlap between the color channels of the camera. For two target spot case, the green and the blue frequency bands were collected together on the same target spot. These two boost each other to compete the concentration of the red frequency that has a high-valued spectral response. The data for two target spots yield better results than the data for three target spots as to spectral splitting ratios as well. In addition to the overlapping frequencies, the algorithm is designed primarily to increase the frequency bands' concentration. These are the reasons why the results of the two target spots are better. A multi-spectral camera can be used to prevent overlapping frequencies, and weight functions to smoothen the spectral responses.

Actually, wavelength dependence does not only arise from the sensing mechanism. It can be decreased by using high phase responses in SLM. However, fluctuations in the phase response would increase in that way.



## CHAPTER 5

### CONCLUSION

In this study, we utilized the experimental methods to create CGHs that can eventually be turned into physical SpliCons that are able to both spectrally split and concentrate the broadband light. Compared with the conventional numerical methods adopted, we conducted an experiment using SLM to adjust the phases on the diffraction plane by wavefront shaping. We take advantage of real-life parameters, but the source's spatial coherence that we used differs from the sunlight to some extent. However, the method that we use here can be applied to sunlight by imitating the sun's spectral degree of coherence with a broadband source [35–39]. We exploited a specified polarization axis dictated by the SLM. Our approach might be generalized to modulate the light with different polarization axes, which will eventually increase the spectral splitting ratio and the enhancement factor [40]. Another method to increase these metrics is to increase the adjustable superpixels on the SLM, as we have shown. To generalize, we can state that any method that can provide us with an extra degree of freedom helps us increase the spectral splitting ratio and the enhancement factor. Increasing adjustable superpixel numbers as well as decreasing superpixel size, i.e., increasing pixel density, are some examples of an increased degree of freedom. However, we kept the pixel density and size achievable by the current fabrication methods that provide large scale production of SpliCons. We predict that the decreasing optimization time ( $\sim 300\times$ ) and the designing ability of SpliCons in real-life conditions will give rise to creating tandem cells with particular geometries and materials.



## REFERENCES

- [1] F. L. Camera, ed., *Renewable Power Generation Costs in 2019*, (International Renewable Energy Agency, Abu Dhabi), IRENA (2020), 2020.
- [2] Holoeye, HOLOEYE Photonics AG Volmerstrasse 1 12489 Berlin, Germany, *Pluto-2 Phase Only Spatial Light Modulators*, 1.7 ed., 8 2018.
- [3] G. Pearson, D. Chapin, and C. Fuller, “Bell labs demonstrates the first practical silicon solar cell,” *American Physical Society (APS News)*, vol. 18, no. 4, 1954.
- [4] J. F. Geisz, R. M. France, K. L. Schulte, M. A. Steiner, A. G. Norman, H. L. Guthrey, M. R. Young, T. Song, and T. Moriarty, “Six-junction iii–v solar cells with 47.1% conversion efficiency under 143suns concentration,” *Nature Energy*, vol. 5, p. 326–335, 4 2020.
- [5] A. Mojiri, R. Taylor, E. Thomsen, and G. Rosengarten, “Spectral beam splitting for efficient conversion of solar energy — a review,” *Renewable and Sustainable Energy Reviews*, vol. 28, pp. 654 – 663, 2013.
- [6] M. Stefancich, A. Zayan, M. Chiesa, S. Rampino, D. Roncati, L. Kimerling, and J. Michel, “Single element spectral splitting solar concentrator for multiple cells CPV system,” *Opt. Express*, vol. 20, pp. 9004–9018, Apr 2012.
- [7] M. B. Fleming and M. C. Hutley, “Blazed diffractive optics,” *Appl. Opt.*, vol. 36, pp. 4635–4643, Jul 1997.
- [8] N. Streibl, “Diffractive optical elements for optoelectronic interconnections,” in *Intl Colloquium on Diffractive Optical Elements* (J. Nowak and M. Zajac, eds.), vol. 1574, pp. 34 – 47, International Society for Optics and Photonics, SPIE, 1991.
- [9] J. W. Goodman, *Introduction to Fourier Optics*. 4950 S. Yosemite Street, F2 197 Greenwood Village, CO 80111 UNITED STATES: Roberts & Company Publishers, 3 ed., 2005.

- [10] E. Stankevičius, P. Gecys, M. Gedvilas, C. Bischoff, E. Jäger, U. Umhofer, F. Voelklein, and G. Raciukaitis, “Laser processing by using diffractive optical laser beam shaping technique,” *Journal of Laser Micro/Nanoengineering*, vol. 6, 03 2011.
- [11] Q. A. Abdullah, “A star is born: The state of new lidar technologies,” *Photogrammetric Engineering Remote Sensing*, vol. 82, no. 5, pp. 307 – 312, 2016.
- [12] G. N. Nguyen, *Modeling, design and fabrication of diffractive optical elements based on nanostructures operating beyond the scalar paraxial domain*. PhD thesis, Université de Bretagne Occidentale, Technopôle Brest-Iroise CS 83818 29238 Brest cedex 03, 2 2014.
- [13] R. Gerchberg and W. Saxton, “A practical algorithm for the determination of phase from image and diffraction plane pictures,” *Optik*, vol. 35, pp. 237–250, 1972.
- [14] G. Z. Yang, B. Z. Dong, B. Y. Gu, J. Y. Zhuang, and O. K. Ersoy, “Gerchberg-Saxton and Yang-Gu algorithms for phase retrieval in a nonunitary transform system: a comparison,” *Appl. Opt.*, vol. 33, pp. 209–218, Jan 1994.
- [15] M. A. Seldowitz, J. P. Allebach, and D. W. Sweeney, “Synthesis of digital holograms by direct binary search,” *Appl. Opt.*, vol. 26, pp. 2788–2798, Jul 1987.
- [16] M. Skeren, I. Richter, and P. Fiala, “Iterative Fourier transform algorithm: different approaches to diffractive optical element design,” in *Laser Beam Shaping III* (F. M. Dickey, S. C. Holswade, and D. L. Shealy, eds.), vol. 4770, pp. 75 – 88, International Society for Optics and Photonics, SPIE, 2002.
- [17] G. Zhou, Y. Chen, Z. Wang, and H. Song, “Genetic local search algorithm for optimization design of diffractive optical elements,” *Appl. Opt.*, vol. 38, pp. 4281–4290, Jul 1999.
- [18] Y. Lin, T. J. Kessler, and G. N. Lawrence, “Design of continuous surface-relief phase plates by surface-based simulated annealing to achieve control of focal-plane irradiance,” *Opt. Lett.*, vol. 21, pp. 1703–1705, Oct 1996.

- [19] A. Yolalmaz and E. Yüce, “Effective bandwidth approach for the spectral splitting of solar spectrum using diffractive optical elements,” *Opt. Express*, vol. 28, pp. 12911–12921, Apr 2020.
- [20] G. Kim, J. A. Dominguez-Caballero, H. Lee, D. J. Friedman, and R. Menon, “Increased photovoltaic power output via diffractive spectrum separation,” *Phys. Rev. Lett.*, vol. 110, p. 123901, Mar 2013.
- [21] H. Yu, K. Lee, and Y. Park, “Ultrahigh enhancement of light focusing through disordered media controlled by mega-pixel modes,” *Opt. Express*, vol. 25, pp. 8036–8047, Apr 2017.
- [22] J. Leach, G. Sinclair, P. Jordan, J. Courtial, M. J. Padgett, J. Cooper, and Z. J. Laczik, “3d manipulation of particles into crystal structures using holographic optical tweezers,” *Opt. Express*, vol. 12, pp. 220–226, Jan 2004.
- [23] C. Maurer, A. Jesacher, S. Bernet, and M. Ritsch-Marte, “What spatial light modulators can do for optical microscopy,” *Laser & Photonics Reviews*, vol. 5, no. 1, pp. 81–101, 2011.
- [24] Z. Kuang, W. Perrie, J. Leach, M. Sharp, S. P. Edwardson, M. Padgett, G. Dearn, and K. G. Watkins, “High throughput diffractive multi-beam femtosecond laser processing using a spatial light modulator,” *Applied Surface Science*, vol. 255, no. 5, Part 1, pp. 2284 – 2289, 2008.
- [25] P. A. Krulevitch, P. A. Bierden, T. Bifano, E. Carr, C. E. Dimas, H. Dyson, M. A. Helmbrecht, P. Kurczynski, R. S. Muller, S. S. Olivier, Y.-A. Peter, B. Sadoulet, O. Solgaard, and E.-H. Yang, “MOEMS spatial light modulator development at the Center for Adaptive Optics,” in *MOEMS and Miniaturized Systems III* (J. H. Smith, ed.), vol. 4983, pp. 172 – 179, International Society for Optics and Photonics, SPIE, 2003.
- [26] A. M. Weiner, “Femtosecond pulse shaping using spatial light modulators,” *Review of Scientific Instruments*, vol. 71, no. 5, pp. 1929–1960, 2000.
- [27] F. Mok, J. Diep, H.-K. Liu, and D. Psaltis, “Real-time computer-generated hologram by means of liquid-crystal television spatial light modulator,” *Opt. Lett.*, vol. 11, pp. 748–750, Nov 1986.

- [28] I. M. Vellekoop and A. P. Mosk, “Focusing coherent light through opaque strongly scattering media,” *Opt. Lett.*, vol. 32, pp. 2309–2311, Aug 2007.
- [29] E. Hecht, *Optics*. Edinburgh Gate Harlow Essex CM20 2JE England: Pearson Education, 5 ed., 2017.
- [30] D. Gabor, “A new microscopic principle,” *Nature*, vol. 161, pp. 777–778, 5 1948.
- [31] B. R. Brown and A. W. Lohmann, “Complex spatial filtering with binary masks,” *Appl. Opt.*, vol. 5, pp. 967–969, Jun 1966.
- [32] S. Stuerwald, *Digital Holographic Methods*, vol. 221. Springer, 2018.
- [33] Thorlabs, *SLS201L(/M) Stabilized Tungsten Light Sources User Guide*, 1 2020.
- [34] Allied Vision, Allied Vision Technologies GmbH Taschenweg 2a, 07646 Stadtroda / Germany, *Guppy PRO Technical Manual*, 4.1.5 ed., 2 2019.
- [35] S. Divitt and L. Novotny, “Spatial coherence of sunlight and its implications for light management in photovoltaics,” *Optica*, vol. 2, pp. 95–103, Feb 2015.
- [36] Y. Deng and D. Chu, “Coherence properties of different light sources and their effect on the image sharpness and speckle of holographic displays,” *Scientific Reports*, vol. 7, p. 5893, Feb 2017.
- [37] A. T. Friberg and E. Wolf, “Relationships between the complex degrees of coherence in the space–time and in the space–frequency domains,” *Opt. Lett.*, vol. 20, pp. 623–625, Mar 1995.
- [38] H. Mashaal and J. M. Gordon, “Fundamental bounds for antenna harvesting of sunlight,” *Opt. Lett.*, vol. 36, pp. 900–902, Mar 2011.
- [39] H. Mashaal, A. Goldstein, D. Feuermann, and J. M. Gordon, “First direct measurement of the spatial coherence of sunlight,” *Opt. Lett.*, vol. 37, pp. 3516–3518, Sep 2012.
- [40] J. Liu and J. Wang, “Demonstration of polarization-insensitive spatial light modulation using a single polarization-sensitive spatial light modulator,” *Scientific Reports*, vol. 5, p. 9959, 07 2015.